Comput Mech (2013) 52:1445–1462
DOI 10.1007/s00466-013-0886-z

ORIGINAL PAPER

A meshfree weak-strong (MWS) form method for the unsteady magnetohydrodynamic (MHD) flow in pipe with arbitrary wall conductivity

Mehdi Dehghan · **Rezvan Salehi**

Received: 14 February 2013 / Accepted: 20 May 2013 / Published online: 13 July 2013

Abstract In this paper a meshfree weak-strong (MWS) form method is considered to solve the coupled equations in velocity and magnetic field for the unsteady magnetohydrodynamic flow throFor this modified estimaFor this modified estimaFor this modified estimaugh a pipe of rectangular and circular sections having arbitrary conducting walls. Computations have been performed for various Hartman numbers and wall conductivity at different time levels. The MWS method is based on applying a meshfree collocation method in strong form for interior nodes and nodes on the essential boundaries and a meshless local Petrov–Galerkin method in weak form for nodes on the natural boundary of the domain. In this paper, we employ the moving least square reproducing kernel particle approximation to construct the shape functions. The numerical results for sample problems compare very well with steady state solution and other numerical methods.

Keywords Unsteady magnetichydrodynamic flow · Meshfree method · Weak-strong form · Meshless local Petrov–Galerkin method · Moving least square reproducing kernel particle (MLSRKP) approximation

1 Introduction

In recent decades, the finite element method, the finite volume method and the finite difference method (FDM) [11] have been facing some difficulties due to increasing requirements for simulating more and more complicated natural problems. In these methods based on meshes, the global meshing difficulties and a large number of re-meshes in successive computational steps lead to the complexity of the computer program. Meshless methods, as alternative numerical approaches have attracted much attention in the past decade. The main objective of the meshless methods is to get rid of, or at least alleviate the difficulty of, meshing and re-meshing the entire structure, by only adding or deleting nodes in the entire structure, instead. Meshless methods [12,15,51,54] may also alleviate some other problems associated with the finite element method, such as locking, element distortion, and others [32,62].

Some meshfree methods have been developed, such as smooth particle hydrodynamics (SPH) methods [23], diffuse element method (DEM) [44], element free Galerkin method (EFG) [7], reproducing kernel particle method (RKPM) [25,34–36,38], hp- clouds [21], partition of unity method (PUM) [43], meshless local Petrov–Galerkin method (MLPG) [2–5], finite point method [45,55] and so on.

The meshfree collocation strong form method, is a truly meshless method which is easy to implement and computationally efficient but in problems with Neumann boundary conditions is unstable and inaccurate. Moreover, the meshfree weak form methods are accurate and stable approaches that naturally dealt with the Neumann boundary conditions. In spite of this, employing the background cells for numerical integration makes the weak form method not totally meshfree and computationally expensive. Considering the above stated matters, Liu and Gu [39,40] introduced the meshfree weak-strong form (MWS) method based on a combination of strong form and local Petrov–Galerkin weak form of Atluri [3]. The aim of the MSW method is to remove the quadrature cells as much as possible and still achieve an accurate and

M. Dehghan (✉) · R. Salehi
Department of Applied Mathematics, Faculty of Mathematics and Computer Science, Amirkabir University of Technology, No. 424, Hafez Ave., 15914 Tehran, Iran
e-mail: mdehghan.aut@gmail.com; mdehghan@aut.ac.ir

R. Salehi
e-mail: rsalehi@aut.ac.ir

stable numerical procedure. The MWS method has been successfully developed and applied for the static and dynamic analysis of structures [16,17,26,39–41,63]. The method uses the moving least square approximation [47] or radial point interpolation [17] to construct the shape functions for the collocation method and employs them for internal nodes and nodes on the essential boundaries while applies the meshless local Petrov–Galerkin method for nodes on natural boundary of the problem domain.

Magnetohydrodynamic (MHD) equation studies the interaction between the flow of an electrically conducting fluid and magnetic fields. Faraday first pointed out an interaction of sea flows with the earth as magnetic field (1832). In the beginning of the 20th century the first proposals for applying electromagnetic induction phenomenon in technical devices with electrically-conducting liquids and gases appeared. Systematic studies of magnetohydrodynamic (MHD) flows began in the 30s when the first exact solutions of MHD equations were obtained and experiments on liquid metal flows in MHD channels were performed by Hartmann and Lazarus [29]. The discovery of Alfvén waves finalized the establishment of magnetohydrodynamic as an individual science for which he received the Nobel Prize in Physics (1970) [1]. The study of flow of conducting fluids in the presence of magnetic fields has attracted owning to its applications in the evolution and dynamics of astrophysical objects, thermonuclear fusion, metallurgy and semiconductor crystal growth, etc.

The set of equations which describe MHD are a combination of the Navier–Stokes equations of fluid dynamics and Maxwell's equations of electromagnetism. Due to this, the equations governing MHD are rather cumbersome and exact solutions are available only for simple geometry subject to simple boundary conditions [10,20,24,28,49]. Gupta and Singh [27] obtained exact solution for unsteady flows in some special cases. Hence, some numerical methods have been applied to give the approximate solution for the MHD flow problems. For numerical research on MHD flow, we can refer to works of Singh and Lal [52,53] by finite element method for Hartmann numbers less than 10, Tezer–Sezgin and Köksal [56] by finite element method for moderate Hartmann numbers, Sheu and Lin [50] by finite difference method, Tezer–Sezgin and Bozkaya [59], Tezer-Sezgin [57], Tezer-Sezer and Aydin [58], and Hosseinzadeh et al. [30] by boundary element method [30] and dual reciprocity boundary element method, stablized finite element method by Salah et al. [46], Veradi et al. [60,61] by element free Galerkin method, Shakeri and Dehghan [48] by a combination of finite volume and spectral element method, Dehghan and Mirzaei [13] by meshless local boundary integral equation method, Dehghan and Mirzaei [14] by meshless local Petrov–Galerkin method. Some other research works can be found in [9,8,42].

In the current paper, the meshfree weak-strong form method is applied to numerically solve the unsteady MHD flow with arbitrarily conducting walls. We consider pipes of rectangular and circular cross-sections to demonstrate the numerical method. For different Hartmann number and wall conductivity, the velocity and induced magnetic field have been computed at various time levels. In the current work, we employed the MLSRKP approximation to obtain the shape functions.

The reminder of this paper is structured as follows: In Sect. 2, the governing equations of the studied problem are presented. A brief discussion of the moving least reproducing kernel particle (MLSRKP) approximation is presented in Sect. 3. In Sect. 4, a time stepping method and numerical implementation of the method are demonstrated. Section 5 includes some test problems and comparisons to reveal the efficiency and accuracy of the proposed method. Finally, some concluding remarks are drawn in Sect. 6.

2 Governing equation

The set of equations which describe MHD are a combination of the Navier–Stokes equations of fluid dynamics and Maxwell's equations of electromagnetism. For viscous and incompressible fluid, the governing equations in the flow region are [53,61]

$$\rho\frac{\partial V_Z}{\partial T}-KF(T)=\acute{\eta}\nabla^2 V_Z+\frac{B_0}{\mu_0}\left(\cos(\theta)\frac{\partial B_Z}{\partial X}+\sin(\theta)\frac{\partial B_Z}{\partial Y}\right), \tag{2.1}$$

$$\frac{\partial B_Z}{\partial T}=\frac{1}{\mu_0\sigma}\nabla^2 B_Z+B_0\left(\cos(\theta)\frac{\partial V_Z}{\partial X}+\sin(\theta)\frac{\partial V_Z}{\partial Y}\right), \tag{2.2}$$

where

ρ, $\acute{\eta}$, σ density, viscosity and conductivity of fluid,
μ_0 a constant $= 4\pi \times 10^{-7}$ in MKS, system,
T time variable,
θ orientation of applied magnetic filed with X-axis,
B_0 applied magnetic filed,
V_Z, B_z axial velocity and induced magnetic field,
$-KF(T)$ pressure gradient,
∇^2 is the two-dimensional Laplacian operator.

The boundary conditions on V_Z and B_Z are

$$V_Z=0,\qquad \frac{\partial B_Z}{\partial \vec{N}}+\frac{\sigma}{\acute{\sigma}}\frac{B_Z}{\acute{h}}=0, \tag{2.3}$$

where $\vec{N}$ is the outward normal to the boundary of the domain, $\acute{\sigma}$ and $\acute{h}$ are the wall conductance and the small wall thickness, respectively.

The initial conditions depend upon how the motion starts initially. If initially the fluid is rest and the motion starts by applying the constant pressure, then the initial conditions become

$$V_Z(X, Y, 0) = 0, \qquad B_Z(X, Y, 0) = 0. \tag{2.4}$$

Considering the non–dimensional variables and parameters by

$$V = \frac{V_Z}{V_0}, \qquad V_0 = \frac{Ka^2}{\acute{\eta}}, \qquad B = \frac{B_Z}{V_0\mu_0\sqrt{\sigma\acute{\eta}}},$$
$$x = \frac{X}{a}, \quad y = \frac{Y}{a}, \quad M^2 = \frac{B_0^2a^2\sigma}{\acute{\eta}}, \quad \lambda = \frac{\sigma a}{\acute{\sigma}\acute{h}},$$
$$R = \frac{\rho a V_0}{\acute{\eta}}, \qquad R_m = V_0 a\mu_0\sigma, \qquad t = \frac{TV_0}{a},$$
$$f(t) = F\left(\frac{aT}{V_0}\right),$$

where M, R and R_m are the Hartmann number, Reynolds number and magnetic Reynolds number, respectively. Then the governing equations are reduced to

$$R\frac{\partial V}{\partial t} - f(t) = \nabla^2 V + M\left(\cos(\theta)\frac{\partial B}{\partial x} + \sin(\theta)\frac{\partial B}{\partial y}\right), \tag{2.5}$$

$$R_m\frac{\partial B}{\partial t} = \nabla^2 B + M\left(\cos(\theta)\frac{\partial V}{\partial x} + \sin(\theta)\frac{\partial V}{\partial y}\right), \tag{2.6}$$

in $\Omega \times [0, \infty)$ with boundary conditions

$$V = 0, \quad \text{on } \partial\Omega, \tag{2.7}$$
$$\frac{\partial B}{\vec{n}} + \lambda B = 0, \quad \text{on } \partial\Omega, \tag{2.8}$$

and initial conditions

$$V(x, y, 0) = B(x, y, 0) = 0, \quad (x, y) \in \Omega, \tag{2.9}$$

where Ω represents the section of the pipe in the non–dimensional form with boundary $\partial\Omega$.

In the limiting case of perfectly insulating ($\acute{\sigma} = 0, \lambda = \infty$) and conducting ($\acute{\sigma} = \infty, \lambda = 0$) walls, the boundary conditions become $V = B = 0$ and $V = \frac{\partial B}{\partial \vec{n}} = 0$, respectively [27].

3 Approximation in the MWS form method

The classical MWS form method employs the moving least square approximation and radial point interpolation method to approximate the unknown function. In the current work, we make the approximation by moving least square reproducing kernel particle (MLSRKP) [33,37]. The MLSRKP was provided as a different version of the moving last square (MLS) approximation where the shape functions are generated by a MLS process. The interpolation of this kind contains a reproducing kernel (RK), which, as a generalization of the discrete case, establishes a continuous basis for a partition of unity and can reproduce any smooth function accurately in a global least square sense. Now we give an outline of this method.

Let $u(x), x \in \mathbb{R}^d$, be a sufficiently smooth function defined on a simply open set $\Omega \subset \mathbb{R}^d$ with a Lipschitz continuous boundary. For each $x \in \overline{\Omega}$, we define

$$\mathcal{B}(x) = \left\{y \in \Omega | \varphi\left(\frac{x-y}{\rho}\right) \neq 0\right\} \subseteq \Omega. \tag{3.1}$$

Also, for a positive integer m, the space of polynomials of degree $\leq m$ in $\mathbb{R}^d$ is defined as

$$\mathcal{P}_{m,d} = \mathrm{span}\{(x-y)^\alpha\}_{\alpha:\,|\alpha|\leq m}, \tag{3.2}$$

and define $u_x : \mathcal{B}(x) \to \mathbb{R}$ by

$$\forall y \in \mathcal{B}(x), \quad u_x(y) = u(y). \tag{3.3}$$

The process of finding the global approximating function $u^G : \Omega \to \mathbb{R}$ is that at each point $\bar{x} \in \Omega$, by employing the concept of the inner product a local approximant $L_{\bar{x}}u : \mathcal{B}(\bar{x}) \to \mathbb{R}$ for function $u_{\bar{x}} : \Omega \to \mathbb{R}$ is obtained. Then the global approximant is obtained as follows:

$$u^G(x) := \lim_{\bar{x}\to x}(L_{\bar{x}}u)(x), \qquad \forall x \in \overline{\Omega}. \tag{3.4}$$

In the current contribution, for a fixed point $\bar{x} \in \bar{\Omega}$, the local approximant is considered as follows:

$$\begin{aligned} u^l(x) \cong (Lu_{\bar{x}})(x) &:= \sum_{i=1}^{Q}\psi_i\left(\frac{x-\bar{x}}{\rho}\right)d_i(\bar{x}) \\ &= \Psi\left(\frac{x-\bar{x}}{\rho}\right)\mathbf{d}(\bar{x}), \end{aligned} \tag{3.5}$$

where $Q = \dim\mathcal{P}_{m,d} = \begin{pmatrix} m+d \\ d \end{pmatrix}$ and

$$\mathbf{d}^t(y) := \{d_1, d_2, \ldots, d_Q\}(y), \tag{3.6}$$
$$\Psi(y) := \{p_1, p_2, \ldots, p_Q\}, \tag{3.7}$$
$$p_i = \frac{(x-y)^{\alpha_i}}{\rho}, \quad i = 1, 2, \ldots, m. \tag{3.8}$$

Since the polynomial series is finite, then we can define a residual r_ρ

$$r_\rho := u^l(x) - \Psi\left(\frac{x-\bar{x}}{\rho}\right)\mathbf{d}(\bar{x}), \quad x \in \mathcal{B}(\bar{x}). \tag{3.9}$$

Then a functional related to this residual is defined as

$$\mathcal{J}(\mathbf{d}(\bar{x})) = \int_{\mathcal{B}(\bar{x})} r_\rho^2(x, \bar{x})\omega_\rho(x-\bar{x})\,d\mathcal{B}, \tag{3.10}$$

where $\omega_\rho(x-\bar{x}) = \omega(\frac{x-\bar{x}}{\rho})$. One can obtain the following equation by minimizing the quadratic form $\mathcal{J}(\mathbf{d}(\bar{x}))$

$$\int_{\mathcal{B}(\bar{x})}\Psi^t\left(\frac{x-\bar{x}}{\rho}\right)\left(u^l(x) - \Psi\left(\frac{x-\bar{x}}{\rho}\right)\mathbf{d}(\bar{x})\right)\omega_\rho(x-\bar{x})\,d\mathcal{B} = 0. \tag{3.11}$$

When $\operatorname{supp}\{\omega_\rho(x-\bar{x})\} \subseteq \overline{\mathcal{B}}$, then the above integral can be extended over the whole domain

$$\int_{\Omega_x} \Psi^t\left(\frac{x-\bar{x}}{\rho}\right)(u^l(x)-\Psi\left(\frac{x-\bar{x}}{\rho}\right)\mathbf{d}(\bar{x}))\omega_\rho(x-\bar{x})\,\mathrm{d}\Omega_x = 0, \tag{3.12}$$

which yields

$$\left(\int_{\Omega_x} \Psi^t\left(\frac{x-\bar{x}}{\rho}\right)\omega_\rho(x-\bar{x})\Psi\left(\frac{x-\bar{x}}{\rho}\right)\mathrm{d}\,\Omega_x\right)\mathbf{d}(\bar{x}) = \int_{\Omega_x} \Psi^t\left(\frac{x-\bar{x}}{\rho}\right)u(x)\omega_\rho(x-\bar{x})\mathrm{d}\,\Omega_x. \tag{3.13}$$

Now, if we define an (Q)–by–(Q) matrix $\mathcal{M}(x)$ as follows:

$$\mathcal{M}(\bar{x}) := \int_{\Omega_x} \Psi^t\left(\frac{x-\bar{x}}{\rho}\right)\omega_\rho(x-\bar{x})\Psi\left(\frac{x-\bar{x}}{\rho}\right)\mathrm{d}\,\Omega_x, \tag{3.14}$$

then the unknown vector $\mathbf{d}(\bar{x})$ is determined as:

$$\mathbf{d}(\bar{x}) = \mathcal{M}^{-1}(\bar{x})\int_{\Omega_x} \Psi^t\left(\frac{x-\bar{x}}{\rho}\right)u(x)\omega_\rho(x-\bar{x})\mathrm{d}\,\Omega_x. \tag{3.15}$$

According to (3.5) and (3.15), we will have

$$\forall x \in \mathcal{B}(\bar{x}) \quad u^l(x) = (L_{\bar{x}}u)(x) = \Psi\left(\frac{x-\bar{x}}{\rho}\right)\mathbf{d}(\bar{x}) = \Psi\left(\frac{x-\bar{x}}{\rho}\right)\mathcal{M}^{-1}(x)\int_{\Omega_y}\Psi^t\left(\frac{y-\bar{x}}{\rho}\right)u(y)\omega_\rho(y-\bar{x})\mathrm{d}\,\Omega_y. \tag{3.16}$$

So, according to relation (3.4), the global approximation function $u^G:\Omega\to\mathbb{R}$ is obtained in the following form:

$$\forall x \in \Omega \quad u^G(x) = (L_x u)(x) = \Psi(0)\mathcal{M}^{-1}(x)\int_{\Omega}\Psi^t\left(\frac{y-x}{\rho}\right)u(y)\omega_\rho(y-x)\mathrm{d}\,\Omega. \tag{3.17}$$

Now, we set

$$\mathcal{C}_\rho(x, x-y) = \Psi(0)\mathcal{M}^{-1}(x)\Psi^t\left(\frac{y-x}{\rho}\right). \tag{3.18}$$

Substituting (3.18) into (3.17), gives

$$\forall x \in \Omega \quad u^G(x) = \int_{\Omega}\mathcal{C}_\rho(x, x-y)u(y)\omega_\rho(y-x)\mathrm{d}\,\Omega. \tag{3.19}$$

Let

$$\mathcal{K}_\rho(x, x-y) = \mathcal{C}_\rho(x, x-y)\omega_\rho(y-x), \tag{3.20}$$

where the function $\mathcal{K}_\rho$ is the so–called reproducing kernel function. Therefore, we will have

$$u(x) := \int_{\Omega}\mathcal{K}_\rho(x, x-y)u(y)\mathrm{d}\,\Omega. \tag{3.21}$$

In order to use (3.21) in the numerical approximation, the integral must be discretized. Let $\{x_i\}_{i=1}^{NP}$, be an admissible particle distribution [37], then by employing the numerical quadrature, one can approximate (3.21) as follows:

$$u(x) = \sum_{i=1}^{NP} u(x_i)\mathcal{C}_\rho^h(x, x_i-x)\omega_\rho(x_i-x)\Delta V_i = \sum_{i=1}^{NP}\mathcal{K}_\rho^h(x, x_i-x)u_i\Delta V_i, \tag{3.22}$$

where ΔV_i denotes the nodal domain associated with the ith particle and

$$\mathcal{C}_\rho^h(x, y-x) = \Psi(0)(\mathcal{M}^h)^{-1}(x)\Psi^t\left(\frac{y-x}{\rho}\right), \tag{3.23}$$

and

$$\mathcal{M}^h(x) = \sum_{i=1}^{NP}\Psi\left(\frac{x_i-x}{\rho}\right)\omega_\rho(x_i-x)\Psi^t\left(\frac{x_i-x}{\rho}\right)\Delta V_i. \tag{3.24}$$

Now, (3.21), can be written as

$$u(x) = \sum_{i=1}^{NP}\mathcal{N}_i^h(\rho, x, x_i)u_i, \tag{3.25}$$

where

$$\mathcal{N}_i^h(\rho, x, x_i) = \mathcal{C}_\rho^h(x, x_i-x)\omega_\rho(x_i-x)\Delta V_i, \tag{3.26}$$

$$= \Psi(0)(\mathcal{M}^h)^{-1}(x)\Psi^t\left(\frac{x_i-x}{\rho}\right)\omega_\rho(x_i-x)\Delta V_i, \tag{3.27}$$

$$= \mathcal{K}_\rho^h(x, x_i-x)\Delta V_i. \tag{3.28}$$

4 The MWS form method implementation

4.1 Time difference approximation

To obtain a fully discrete scheme, the time interval $(0, T_0)$ has been divided into the N uniform subintervals by employing nodes $0 = t_0 \le t_1 \le \cdots \le t_N = T$, where $t_n = n\,\Delta t$, then to deal with the time derivatives, the following difference approximations have been considered

$$\frac{\partial V}{\partial t}(\mathbf{x},t) \simeq \frac{V^{n+1}(\mathbf{x}) - V^n(\mathbf{x})}{\Delta t},$$
$$\frac{\partial B}{\partial t}(\mathbf{x},t) \simeq \frac{B^{n+1}(\mathbf{x}) - B^n(\mathbf{x})}{\Delta t},$$
$$V(\mathbf{x},t) \simeq \frac{V^{n+1}(\mathbf{x}) + V^n(\mathbf{x})}{2},$$
$$B(\mathbf{x},t) \simeq \frac{B^{n+1}(\mathbf{x}) + B^n(\mathbf{x})}{2}, \tag{4.1}$$

where $V^n(\mathbf{x}) = V(\mathbf{x}, n\Delta t)$, $B^n(\mathbf{x}) = B(\mathbf{x}, n\Delta t)$. So, Eqs. (2.5)–(2.6) become as given in the following

$$\frac{R\beta}{2}V^{n+1} - \frac{1}{2}\nabla^2 V^{n+1} - \frac{M}{2}\left(\cos(\theta)\frac{\partial B^{n+1}}{\partial x} + \sin(\theta)\frac{\partial B^{n+1}}{\partial y}\right)$$
$$= f^n + \frac{R\beta}{2}V^n + \frac{1}{2}\nabla^2 V^n + \frac{M}{2}\left(\cos(\theta)\frac{\partial B^n}{\partial x} + \sin(\theta)\frac{\partial B^n}{\partial y}\right), \tag{4.2}$$

$$\frac{R_m\beta}{2}B^{n+1} - \frac{1}{2}\nabla^2 B^{n+1} - \frac{M}{2}\left(\cos(\theta)\frac{\partial V^{n+1}}{\partial x} + \sin(\theta)\frac{\partial V^{n+1}}{\partial y}\right)$$
$$= \frac{R\beta}{2}B^n + \frac{1}{2}\nabla^2 B^n + \frac{M}{2}\left(\cos(\theta)\frac{\partial V^n}{\partial x} + \sin(\theta)\frac{\partial V^n}{\partial y}\right), \tag{4.3}$$

where $\beta = \frac{1}{\Delta t}$.

4.2 The strong form for internal nodes and nodes on essential boundary

Using strong form, the MWS form method yields a system of discretized equations for nodes inside the domain and on essential boundary. Approximating B^n and V^n as (3.25), substituting into Eqs. (4.2) and (4.3) and applying collocation method at each interior point $\mathbf{x}_j$, lead to

$$\frac{R\beta}{2}V_j^{n+1} - \frac{1}{2}\nabla^2 V_j^{n+1} - \frac{M}{2}\left(\cos(\theta)\frac{\partial B_j^{n+1}}{\partial x} + \sin(\theta)\frac{\partial B_j^{n+1}}{\partial y}\right)$$
$$= f_j^n + \frac{R\beta}{2}V_j^n + \frac{1}{2}\nabla^2 V_j^n + \frac{M}{2}\left(\cos(\theta)\frac{\partial B_j^n}{\partial x} + \sin(\theta)\frac{\partial B_j^n}{\partial y}\right), \tag{4.4}$$

$$\frac{R_m\beta}{2}B_j^{n+1} - \frac{1}{2}\nabla^2 B_j^{n+1} - \frac{M}{2}\left(\cos(\theta)\frac{\partial V_j^{n+1}}{\partial x} + \sin(\theta)\frac{\partial V_j^{n+1}}{\partial y}\right)$$
$$= \frac{R\beta}{2}B_j^n + \frac{1}{2}\nabla^2 B_j^n + \frac{M}{2}\left(\cos(\theta)\frac{\partial V_j^n}{\partial x} + \sin(\theta)\frac{\partial V_j^n}{\partial y}\right), \tag{4.5}$$

where

$$B_j^k = B(\mathbf{x}_j, k\Delta t) = \sum_{i=1}^{NP} \mathcal{N}_i(\mathbf{x}_j)\hat{B}_i^n,$$
$$V_j^k = V(\mathbf{x}_j, k\Delta t) = \sum_{i=1}^{NP} \mathcal{N}_i(\mathbf{x}_j)\hat{V}_i^n,$$
$$\frac{\partial B_j^k}{\partial x} = \sum_{i=1}^{NP} \frac{\partial \mathcal{N}_i}{\partial x}(\mathbf{x}_j)\hat{B}_i^k, \quad \frac{\partial B_j^k}{\partial y} = \sum_{i=1}^{NP} \frac{\partial \mathcal{N}_i}{\partial y}(\mathbf{x}_j)\hat{B}_i^k,$$
$$\nabla^2 B_j^k = \sum_{i=1}^{NP}\left(\frac{\partial^2 \mathcal{N}_i}{\partial x^2}(\mathbf{x}_j) + \frac{\partial^2 \mathcal{N}_i}{\partial y^2}(\mathbf{x}_j)\right)\hat{B}_i^k.$$

Also, the boundary conditions (2.7) are imposed as follow

$$\sum_{i=1}^{NP} \mathcal{N}_i(\mathbf{x}_j)\hat{V}_i^{n+1} = 0, \quad \mathbf{x}_j \in \partial\Omega, \tag{4.6}$$

also, in the case of $\lambda = \infty$, the boundary condition (2.8) is imposed similar to (4.6).

4.3 The weak form for nodes on natural boundary condition

In MWS form method, the natural boundary condition is imposed using the local weak form method which is firstly introduced by Atluri and Zhu [3] in the MLPG method. Applying a weighted residual method over each quadrature cell, the MLPG method obtains a local weak form over local sub–domains Ω_s which are small regions considered over each node in the global domain Ω as can be seen in Fig. 1. Therefore, to impose the natural boundary condition (2.8), we consider the following local weak form of (4.2) and (4.3) at each node x_i on the natural boundary (2.8)

$$\int_{\Omega_q^i}\left[\frac{R\beta}{2}V^{n+1} - \frac{1}{2}\nabla^2 V^{n+1} - \frac{M}{2}\left(\cos(\theta)\frac{\partial B^{n+1}}{\partial x} + \sin(\theta)\frac{\partial B^{n+1}}{\partial y}\right)\right]u^*(x)\,d\Omega$$
$$= \int_{\Omega_q^i}\left[f^n + \frac{R\beta}{2}V^n + \frac{1}{2}\nabla^2 V^n + \frac{M}{2}\left(\cos(\theta)\frac{\partial B^n}{\partial x} + \sin(\theta)\frac{\partial B^n}{\partial y}\right)\right]u^*(x)\,d\Omega, \tag{4.7}$$

and

$$\int_{\Omega_q^i}\left[\frac{R_m\beta}{2}B^{n+1} - \frac{1}{2}\nabla^2 B^{n+1} - \frac{M}{2}\left(\cos(\theta)\frac{\partial V^{n+1}}{\partial x} + \sin(\theta)\frac{\partial V^{n+1}}{\partial y}\right)\right]u^*(x)\,d\Omega$$
$$\int_{\Omega_q^i}\left[\frac{R\beta}{2}B^n + \frac{1}{2}\nabla^2 B^n + \frac{M}{2}\left(\cos(\theta)\frac{\partial V^n}{\partial x} + \sin(\theta)\frac{\partial V^n}{\partial y}\right)\right] \times u^*(x)\,d\Omega, \tag{4.8}$$

where $u^*(x)$ is a test function. Employing the divergence theorem and

$$\left[\nabla^2 B\right]u^* = B_{,ll}u^* = \left[B_{,l}u^*\right]_{,l} - B_{,l}u^*_{,l}, \tag{4.9}$$

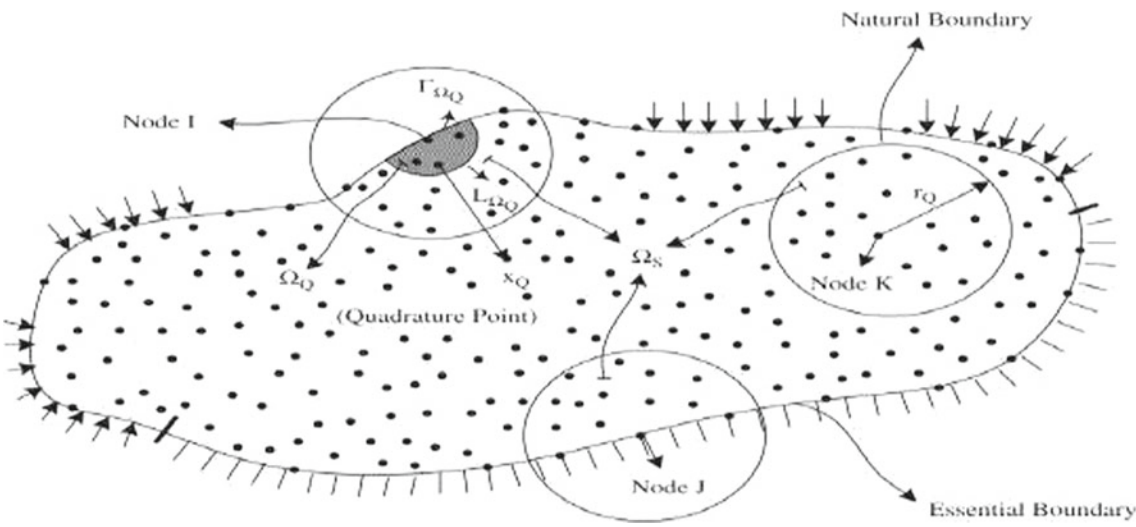

Fig. 1 Local sub-domains and the global domain of the approximation

Table 1 Comparison of velocity field of Shercliff's problem at $M = 5$ using MLPG method [14] FVE method [48], FVSE method [48] and MWS method

(x, y)	Exact value	FVE method $N = 722$	FVSE method $N = 162$	MLPG method $N = 441$	MWS $N = 441$
(0.00, 0.00)	0.171601814	0.170829389	0.171556364	0.170849580	0.171578698
(0.25, 0.00)	0.168372009	0.166994125	0.168326676	0.167642203	0.168344479
(0.50, 0.00)	0.155787639	0.153954518	0.155742364	0.155128896	0.155785003
(0.00, 0.25)	0.164754886	0.160365891	0.164718369	0.164090329	0.164787878
(0.25, 0.25)	0.161621571	0.156257834	0.161585326	0.161035982	0.161651490
(0.50, 0.25)	0.149458308	0.143932112	0.149422849	0.148874152	0.149601572
(0.00, 0.50)	0.141207698	0.132898732	0.141184658	0.140772330	0.141410621
(0.25, 0.50)	0.138504000	0.129751728	0.138481830	0.138115184	0.138704288
(0.50, 0.50)	0.128048264	0.119841829	0.128027365	0.127831234	0.128341303
(0.25, 0.75)	0.089937761	0.080865884	0.089930550	0.089835973	0.089467164
(0.50, 0.75)	0.083498372	0.075216935	0.083492387	0.083378769	0.083964199
(0.75, 0.75)	0.064544256	0.059579241	0.064547312	0.064740823	0.064507588

Equations (4.7) and (4.8) become as follow

$$\begin{aligned}
&\frac{R\beta}{2}\int\limits_{\Omega_q^i} V^{n+1}u^*\,\mathrm{d}\Omega - \frac{1}{2}\int\limits_{\partial\Omega_q^i} V_{,l}^{n+1}n_{,l}u^*\,\mathrm{d}\Gamma + \frac{1}{2}\int\limits_{\Omega_q^i} V_{,l}^{n+1}n_{,l}u_{,l}^*\,\mathrm{d}\Omega\\
&\quad-\frac{M}{2}\int\limits_{\Omega_q^i}\left(\cos(\theta)\frac{\partial B^{n+1}}{\partial x}+\sin(\theta)\frac{\partial B^{n+1}}{\partial y}\right)u^*\,\mathrm{d}\Omega,\\
&\quad=\int\limits_{\Omega_q^i} f^n u^*\,\mathrm{d}\Omega + \frac{R\beta}{2}\int\limits_{\Omega_q^i} V^n u^*\,\mathrm{d}\Omega + \frac{1}{2}\int\limits_{\partial\Omega_q^i} V_{,l}^n n_{,l}u^*\,\mathrm{d}\Gamma\\
&\quad-\frac{1}{2}\int\limits_{\Omega_q^i} V_{,l}^n n_{,l}u_{,l}^*\,\mathrm{d}\Omega + \frac{M}{2}\int\limits_{\Omega_q^i}\left(\cos(\theta)\frac{\partial B^n}{\partial x}+\sin(\theta)\frac{\partial B^n}{\partial y}\right)u^*\,\mathrm{d}\Omega,
\end{aligned}\tag{4.10}$$

and

$$\begin{aligned}
&\frac{R_m\beta}{2}\int\limits_{\Omega_q^i} B^{n+1}u^*\,\mathrm{d}\Omega - \frac{1}{2}\int\limits_{\partial\Omega_q^i} B_{,l}^{n+1}n_{,l}u^*\,\mathrm{d}\Gamma + \frac{1}{2}\int\limits_{\Omega_q^i} B_{,l}^{n+1}n_{,l}u_{,l}^*\,\mathrm{d}\Omega\\
&\quad-\frac{M}{2}\int\limits_{\Omega_q^i}\left(\cos(\theta)\frac{\partial V^{n+1}}{\partial x}+\sin(\theta)\frac{\partial V^{n+1}}{\partial y}\right)u^*\,\mathrm{d}\Omega,\\
&\quad=\frac{R\beta}{2}\int\limits_{\Omega_q^i} B^n u^*\,\mathrm{d}\Omega + \frac{1}{2}\int\limits_{\partial\Omega_q^i} B_{,l}^n n_{,l}u^*\,\mathrm{d}\Gamma - \frac{1}{2}\int\limits_{\Omega_q^i} B_{,l}^n n_{,l}u_{,l}^*\,\mathrm{d}\Omega\\
&\quad+\frac{M}{2}\int\limits_{\Omega_q^i}\left(\cos(\theta)\frac{\partial V^n}{\partial x}+\sin(\theta)\frac{\partial V^n}{\partial y}\right)u^*\,\mathrm{d}\Omega,
\end{aligned}\tag{4.11}$$

Table 2 Comparison of velocity field of Shercliff's problem at $M = 20$ using MLPG method [14] FVE method [48], FVSE method [48] and MWS method

(x, y)	Exact value	FVE method $N_x = N_y = 30$	FVSE method $N_x = N_y = 10$	MLPG method $N = 1681$	MWS $N = 441$
(0.00, 0.00)	0.049918641	0.049949831	0.049904635	0.049921141	0.049906549
(0.25, 0.00)	0.0498802236	0.049931721	0.049866591	0.049883013	0.049865186
(0.50, 0.00)	0.049760102	0.049810629	0.049745566	0.049764512	0.049737697
(0.00, 0.25)	0.049662783	0.04973904	0.049646821	0.049684382	0.049631254
(0.25, 0.25)	0.049570651	0.049653541	0.049555008	0.049593666	0.049537495
(0.50, 0.25)	0.049299034	0.049311106	0.049282439	0.049327163	0.049261090
(0.00, 0.50)	0.047716857	0.047654403	0.047697841	0.047785558	0.047605067
(0.25, 0.50)	0.047452918	0.047395908	0.047434150	0.047520638	0.047346003
(0.50, 0.50)	0.046677531	0.046513455	0.046657809	0.046745300	0.046584030
(0.00, 0.75)	0.037657703	0.037475349	0.037637608	0.037763549	0.037502361
(0.50, 0.75)	0.036166028	0.036002088	0.036145676	0.036262629	0.036025300

Table 3 Numerical solution of velocity for some selected points at different times for non-conducting walls at different times for non-conducting walls and $M = 20$

(x, y)	Numerical method	$t = 0.025$	$t = 0.05$	$t = 0.01$	$t = 0.15$	Steady state
(0.00, 0.00)	MWS	0.02478	0.04387	0.04985	0.04991	0.04992
	CMWS	0.02489	0.04349	0.04987	0.04990	0.04992
(0.50, 0.00)	MWS	0.02293	0.03711	0.04913	0.04976	0.04976
	CMWS	0.02164	0.03487	0.04874	0.04973	0.04976
(0.00, 0.25)	MWS	0.02478	0.04345	0.04958	0.04966	0.04966
	CMWS	0.02488	0.04331	0.04967	0.04968	0.04966
(0.25, 0.25)	MWS	0.02456	0.04178	0.04951	0.04956	0.04957
	CMWS	0.02437	0.04191	0.04985	0.04946	0.04957
(0.50, 0.25)	MWS	0.02281	0.03718	0.04874	0.04929	0.04930
	CMWS	0.02246	0.03450	0.04829	0.04931	0.04930
(0.00, 0.50)	MWS	0.02476	0.04269	0.04768	0.04771	0.04772
	CMWS	0.02467	0.04270	0.04759	0.04779	0.04772
(0.25, 0.50)	MWS	0.02442	0.04052	0.04735	0.04746	0.04745
	CMWS	0.02339	0.03875	0.04693	0.04749	0.04745
(0.50, 0.50)	MWS	0.02279	0.03604	0.04641	0.04666	0.04668
	CMWS	0.02137	0.03374	0.04559	0.04676	0.04668
(0.25, 0.75)	MWS	0.02185	0.03313	0.03719	0.03728	0.03730
	CMWS	0.02137	0.03167	0.03669	0.03724	0.03730

where $\partial\Omega_q$ is the boundary of the local sub-domain Ω_q and for the nodes on the boundary, as one can see in Fig. 1, we have $\partial\Omega_q^i = \Gamma_q^i \bigcup Ł_q^i$. In the MLPG5 method, the test function is taken as Heaviside step function

$$u^* = \begin{cases} 1, & x \in \Omega_s, \\ 0, & x \notin \Omega_s, \end{cases} \tag{4.12}$$

and then $u^*_{,l} = 0$, therefore the local weak form (4.10) and (4.11) are changed into the following integral equations

$$\begin{aligned} &\frac{R\beta}{2}\int\limits_{\Omega_q^i} V^{n+1}\,\mathrm{d}\Omega - \frac{1}{2}\int\limits_{\Gamma_q^i} V_{,l}^{n+1} n_l\,\mathrm{d}\Gamma - \frac{1}{2}\int\limits_{L_q^i} V_{,l}^{n+1} n_l\,\mathrm{d}\Gamma \\ &\quad -\frac{M}{2}\int\limits_{\Omega_q^i}\left(\cos(\theta)\frac{\partial B^{n+1}}{\partial x} + \sin(\theta)\frac{\partial B^{n+1}}{\partial y}\right)\mathrm{d}\Omega \\ &= \int\limits_{\Omega_q^i} f^n\,\mathrm{d}\Omega + \frac{R\beta}{2}\int\limits_{\Omega_q^i} V^n\,\mathrm{d}\Omega + \frac{1}{2}\int\limits_{\Gamma_q^i} V_{,l}^n n_l\,\mathrm{d}\Gamma + \frac{1}{2}\int\limits_{L_q^i} V_{,l}^n n_l\,\mathrm{d}\Gamma \\ &\quad +\frac{M}{2}\int\limits_{\Omega_q^i}\left(\cos(\theta)\frac{\partial B^n}{\partial x} + \sin(\theta)\frac{\partial B^n}{\partial y}\right)\mathrm{d}\Omega, \end{aligned} \tag{4.13}$$

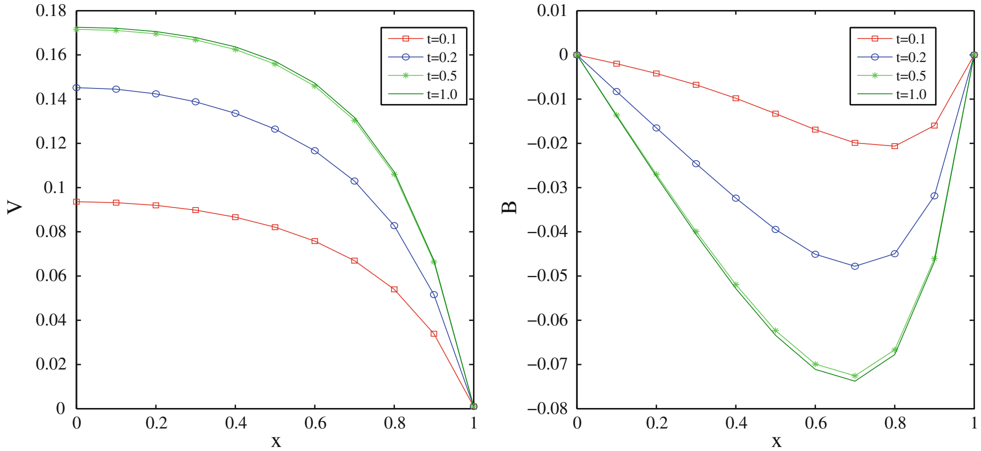

Fig. 2 Velocity and induced magnetic field along the x-axes for $M = 5$ at different time levels

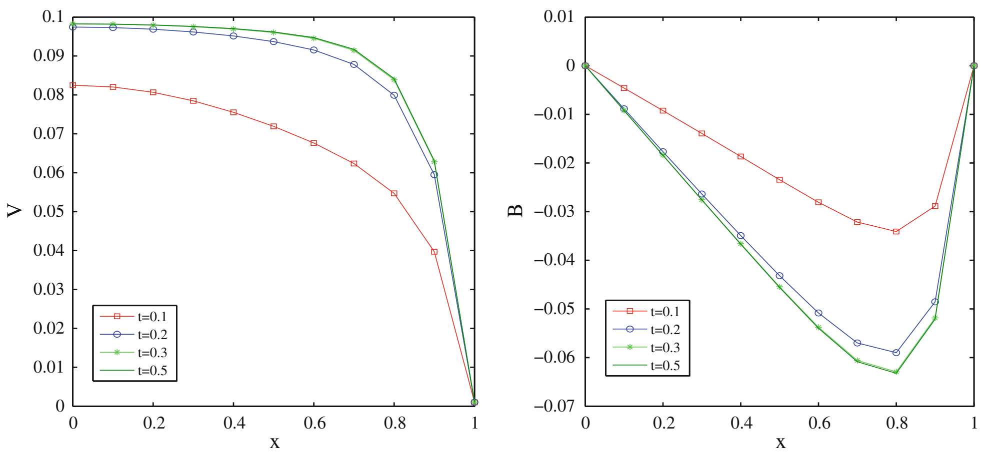

Fig. 3 Velocity and induced magnetic field along the x-axes for $M = 10$ at different time levels

and

$$
\begin{aligned}
&\frac{R_m\beta}{2}\int\limits_{\Omega_q^i} B^{n+1}\,\mathrm{d}\Omega - \frac{1}{2}\int\limits_{\Gamma_q^i} B^{n+1}_{,l} n_l\,\mathrm{d}\Gamma - \frac{1}{2}\int\limits_{L_q^i} B^{n+1}_{,l} n_l\,\mathrm{d}\Gamma \\
&\quad -\frac{M}{2}\int\limits_{\Omega_q^i}\left(\cos(\theta)\frac{\partial V^{n+1}}{\partial x} + \sin(\theta)\frac{\partial V^{n+1}}{\partial y}\right)\mathrm{d}\Omega, \\
&= \frac{R\beta}{2}\int\limits_{\Omega_q^i} B^{n}\,\mathrm{d}\Omega + \frac{1}{2}\int\limits_{\Gamma_q^i} B^{n}_{,l} n_l\,\mathrm{d}\Gamma + \frac{1}{2}\int\limits_{L_q^i} B^{n}_{,l} n_l\,\mathrm{d}\Gamma \\
&\quad +\frac{M}{2}\int\limits_{\Omega_q^i}\left(\cos(\theta)\frac{\partial V^{n}}{\partial x} + \sin(\theta)\frac{\partial V^{n}}{\partial y}\right)\mathrm{d}\Omega. \qquad (4.14)
\end{aligned}
$$

Imposing the natural boundary condition, Eq. (4.14) is transformed into

$$
\begin{aligned}
&\frac{R_m\beta}{2}\int\limits_{\Omega_q^i} B^{n+1}\,\mathrm{d}\Omega + \frac{1}{2}\int\limits_{\Gamma_q^i} \lambda B^{n+1}\,\mathrm{d}\Gamma - \frac{1}{2}\int\limits_{L_q^i} B^{n+1}_{,l} n_l\,\mathrm{d}\Gamma \\
&\quad -\frac{M}{2}\int\limits_{\Omega_q^i}\left(\cos(\theta)\frac{\partial V^{n+1}}{\partial x} + \sin(\theta)\frac{\partial V^{n+1}}{\partial y}\right)\mathrm{d}\Omega, \\
&= \frac{R\beta}{2}\int\limits_{\Omega_q^i} B^{n}\,\mathrm{d}\Omega - \frac{1}{2}\int\limits_{\Gamma_q^i} \lambda B^{n}\,\mathrm{d}\Gamma + \frac{1}{2}\int\limits_{L_q^i} B^{n}_{,l} n_l\,\mathrm{d}\Gamma \\
&\quad +\frac{M}{2}\int\limits_{\Omega_q^i}\left(\cos(\theta)\frac{\partial V^{n}}{\partial x} + \sin(\theta)\frac{\partial V^{n}}{\partial y}\right)\mathrm{d}\Omega. \qquad (4.15)
\end{aligned}
$$

To obtain a discretized system of equations for weak form, we approximate the unknown functions with MLSRKP

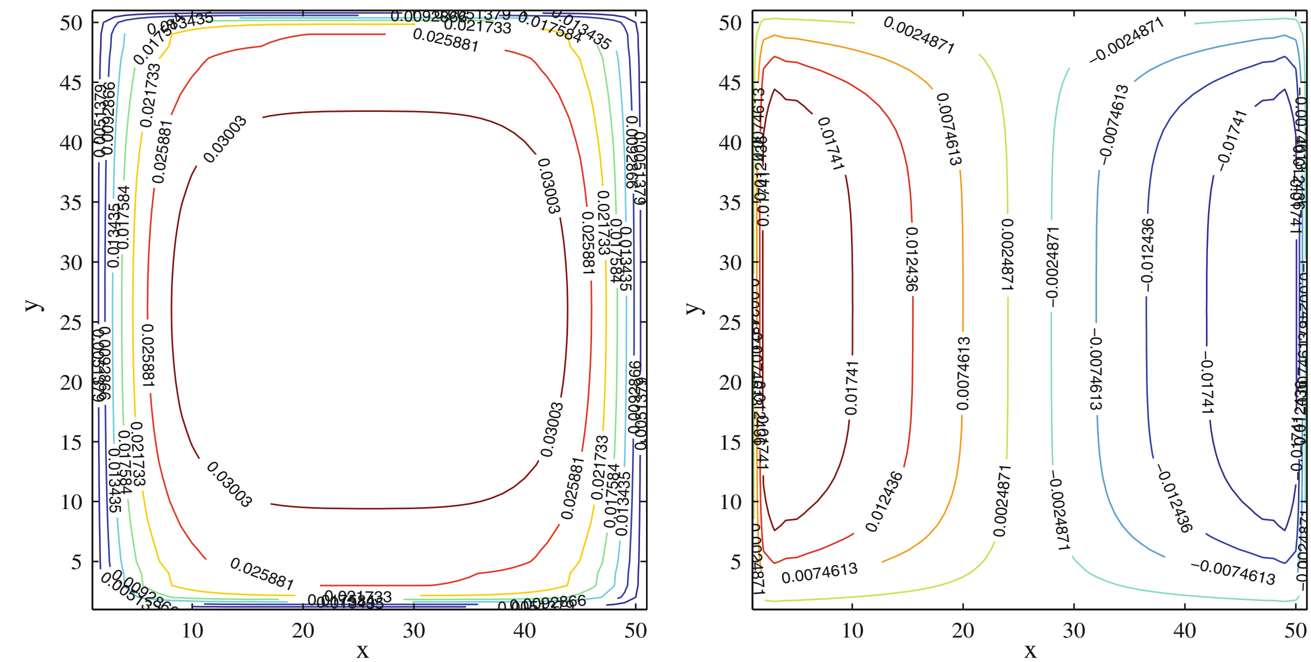

Fig. 4 The contour plots of velocity (*left*) and induced magnetic field (*right*) for $\lambda = \infty$, $M = 30$ at $t = 0.05$ with $N = 1681$

approximation. Substituting the MLSRKP approximation into Eq. (4.15), yields

$$\sum_{j=1}^{NP}\left[\frac{1}{2}K_{ij}+\frac{1}{2}S_{ij}-\frac{1}{2}H_{ij}\right]\hat{B}_j^{n+1}-\frac{M}{2}\sum_{i=1}^{NP}\left[M_{ij}+N_{ij}\right]\hat{V}_j^{n+1}$$
$$=\sum_{j=1}^{NP}\left[\frac{R\beta}{2}K_{ij}+\frac{1}{2}S_{ij}-\frac{1}{2}H_{ij}\right]\hat{B}_j^{n}-\frac{M}{2}\sum_{i=1}^{NP}\left[M_{ij}+N_{ij}\right]\hat{V}_j^{n}, \tag{4.16}$$

where

$$K_{ij}=\frac{R_m\beta}{2}\int_{\Omega_q^i}\mathcal{N}_j(x)\,\mathrm{d}\Omega,\quad S_{ij}=\lambda\int_{\Gamma_q^i}\mathcal{N}_j(x)\,\mathrm{d}\Gamma,$$
$$H_{ij}=\int_{L_q^i}\frac{\partial\mathcal{N}_j}{\partial n}(x)\,\mathrm{d}\Gamma,\quad M_{ij}=\int_{\Omega_q^i}\cos(\theta)\frac{\partial\mathcal{N}_j}{\partial x}(x)\,\mathrm{d}\Omega,$$
$$N_{ij}=\int_{\Omega_q^i}\sin(\theta)\frac{\partial\mathcal{N}_j}{\partial y}(x)\,\mathrm{d}\Omega. \tag{4.17}$$

5 Numerical results

In the test problems, the quadratic basis ($m = 2$) and Gaussian weight function are employed as:

$$w_i(\mathbf{x})=\begin{cases}\frac{\exp[-(d_i/c_i)^2]-\exp[-(r_i/c_i)^2]}{1-\exp[-(r_i/c_i)^2]}, & 0\le d_i\le r_i,\\ 0, & d_i>r_i,\end{cases} \tag{5.1}$$

where $d_i = \|\mathbf{x}-\mathbf{x}_i\|_2$, c_i is a constant controlling the shape of the weight function w_i and r_i is the size of the support domain for node i. Except in the case of circular cross-section, we illustrate our procedure by considering a square pipe $|x| \le 1$, $|y| \le 1$. The calculation has been executed for different values of θ, λ and M. We have $f(t) = 1$ in the case of transient flow with constant pressure gradient. Also, we have taken $R = R_m = 1$.

5.1 Test 1: pipes with non-conducting walls, $\lambda = \infty$ and horizontal magnetic field, $\theta = 0$

As time tends to infinity, the steady state solutions are taken which are founded in special cases. Shercliff [49] obtained the steady solution for the flow in pipes with non-conducting walls with an applied magnetic field parallel to one pair of sides. In this case, these solutions are used to check the accuracy of the results for certain values of Hartmann numbers.

The obtained numerical results by Meshless Local Petrov–Galerkin (MLPG) method [14], Finite Volume Element (FVE) method [48], Finite Volume Spectral Element (FVSE) method [48] and the new method, i.e., Meshfree Weak-Strong (MWS) form method are presented in Tables 1 and 2 for solving the MHD equations with Hartmann numbers $M = 5$ and 20, respectively. From these tables, one can see that the numerical solutions are in a good agreement with steady state solutions, as time increases. Also, a comparison between the present approach and classical MWS (CMWS) with MLS approximation has been provided in Table 3 at different times for $M = 20$.

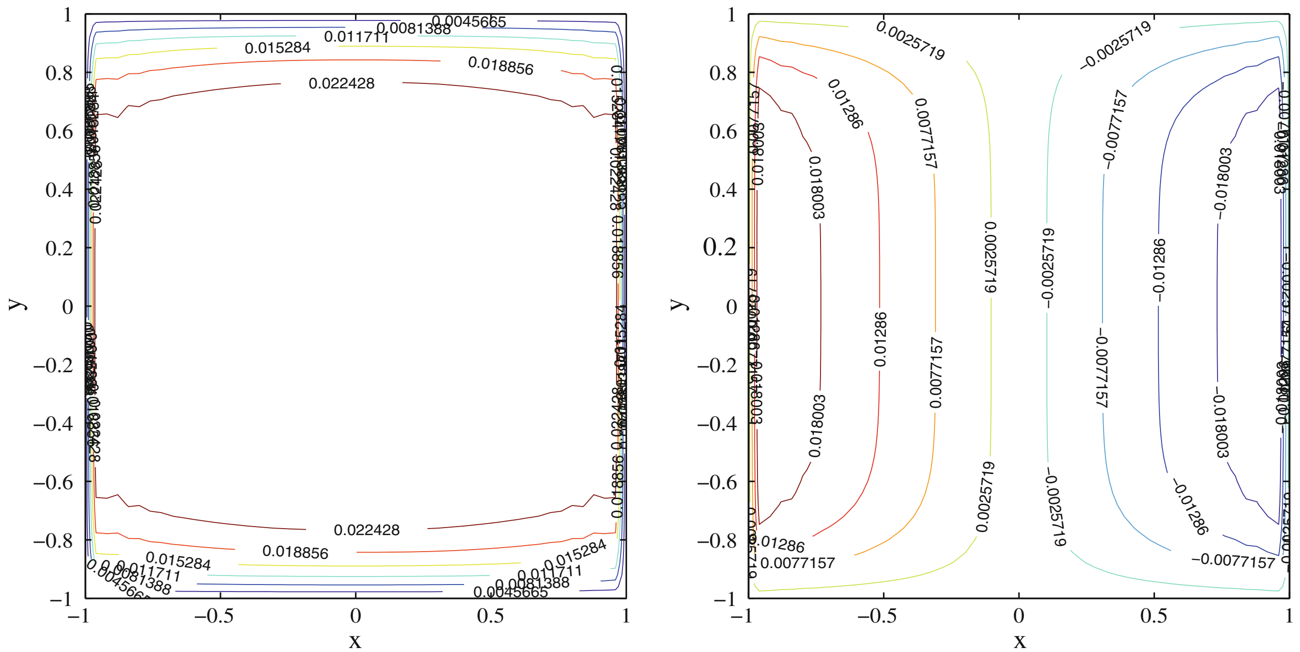

Fig. 5 The contour plots of velocity (*left*) and induced magnetic field (*right*) for $\lambda = \infty$, $M = 40$ at $t = 0.05$ with $N = 1681$

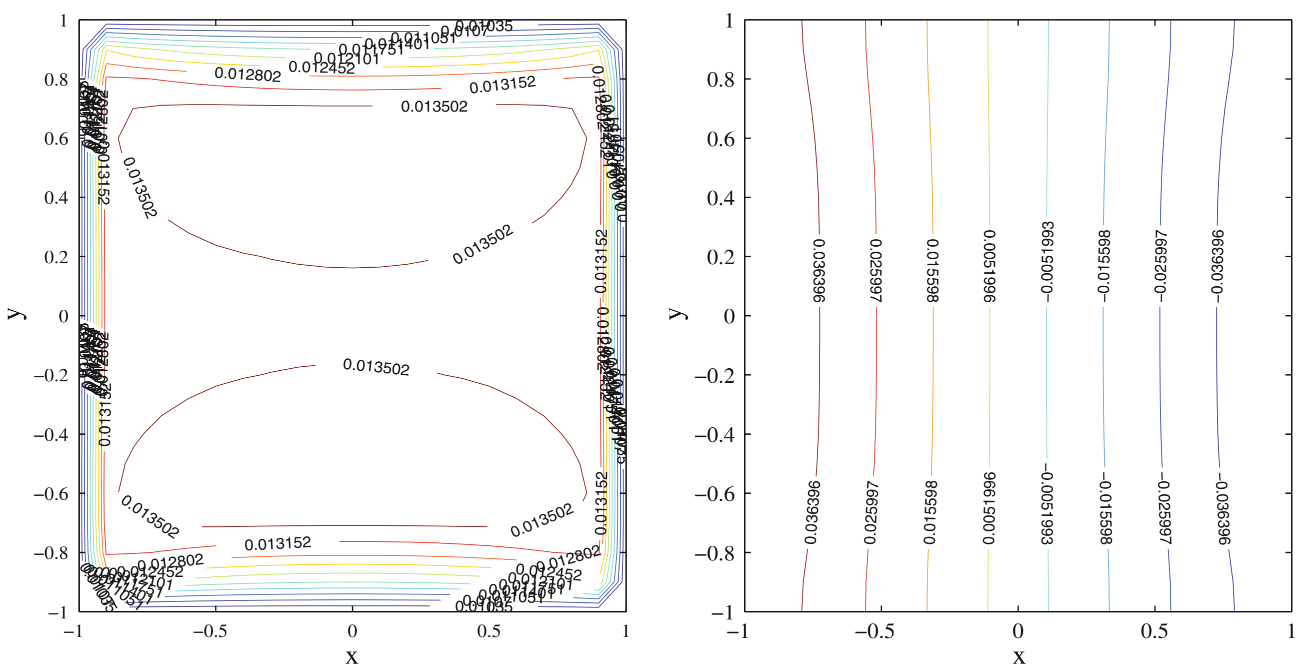

Fig. 6 The contour plots of velocity (*left*) and induced magnetic field (*right*) for $\lambda = 0$, $M = 30$ with $N = 441$

The behaviour of velocity and induced magnetic field along the x-axis, in $y = 0$ plane of the duct, for $M = 5$ and 10 are plotted in Figs. 2 and 3 at several time levels. It can be seen from the figures that the solutions V and B tend to steady state by increasing the times.

The contour plot of velocity and induced magnetic field for different Hartmann numbers $M = 30$ and 40 are depicted in Figs. 4 and 5, respectively. The plots reveal that the velocity is symmetric with respect to both x- and y-axes, but the induced magnetic field is not symmetric with respect to y- axes and therefore the contour lines change their direction in the left and right parts of pipes. Also, these figures show that the boundary layers develop as the Hartmann number increases in both velocity and induced magnetic

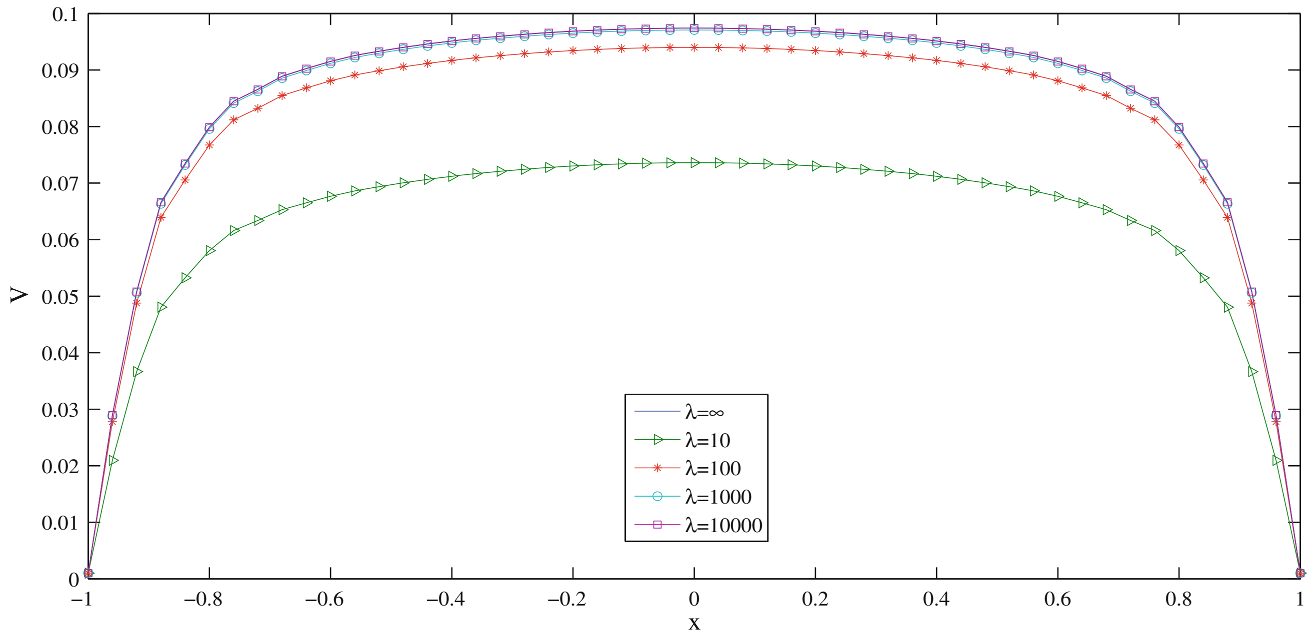

Fig. 7 Graph of velocity along the x-axes ($y = 0$) for $M = 10$, $\theta = 0$ and different values of λ

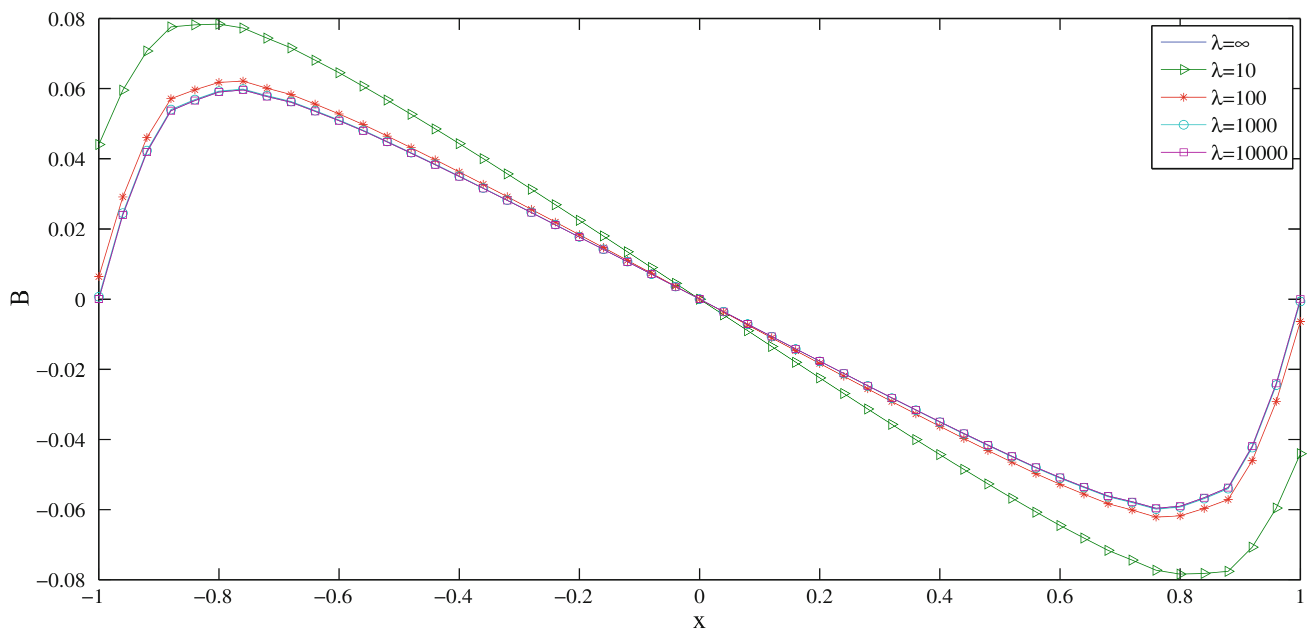

Fig. 8 Graph of induced magnetic field along the x-axes ($y = 0$) for $M = 10$, $\theta = 0$ and different values of λ

field cases. Furthermore, the thickness of boundary layers becomes smaller by increasing the Hartmann number which is the well–known behaviour of MHD duct flow. Finally, in Fig. 13, we depict results for the case of irregular nodal distribution.

5.2 Test 2: ducts with arbitrary wall conductivity $\lambda, 0 \le \lambda < \infty$ and horizontal magnetic field, $\theta = 0$

First of all, we consider $\lambda = 0$ which is the case of MHD flow in a duct with prefect conducting walls of the duct. In

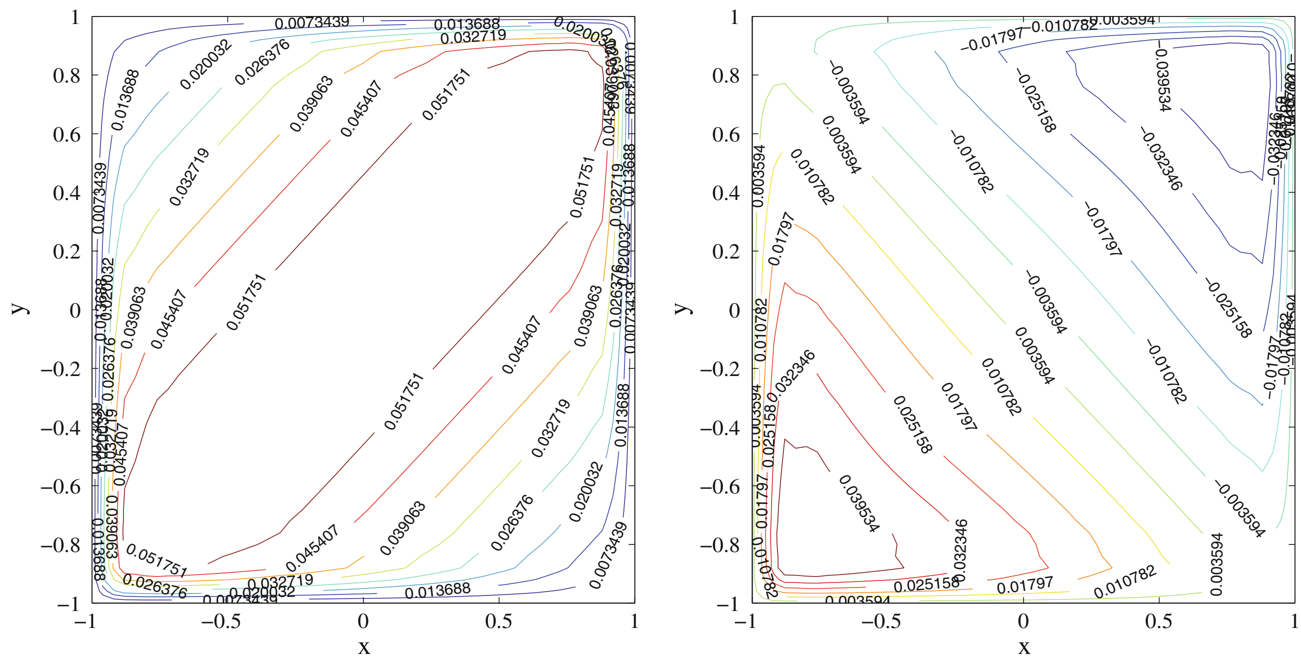

Fig. 9 The contour plot of velocity (*left*) and induced magnetic field (*right*) for $M = 20$, $\lambda = \infty$ and $\theta = \frac{\pi}{4}$

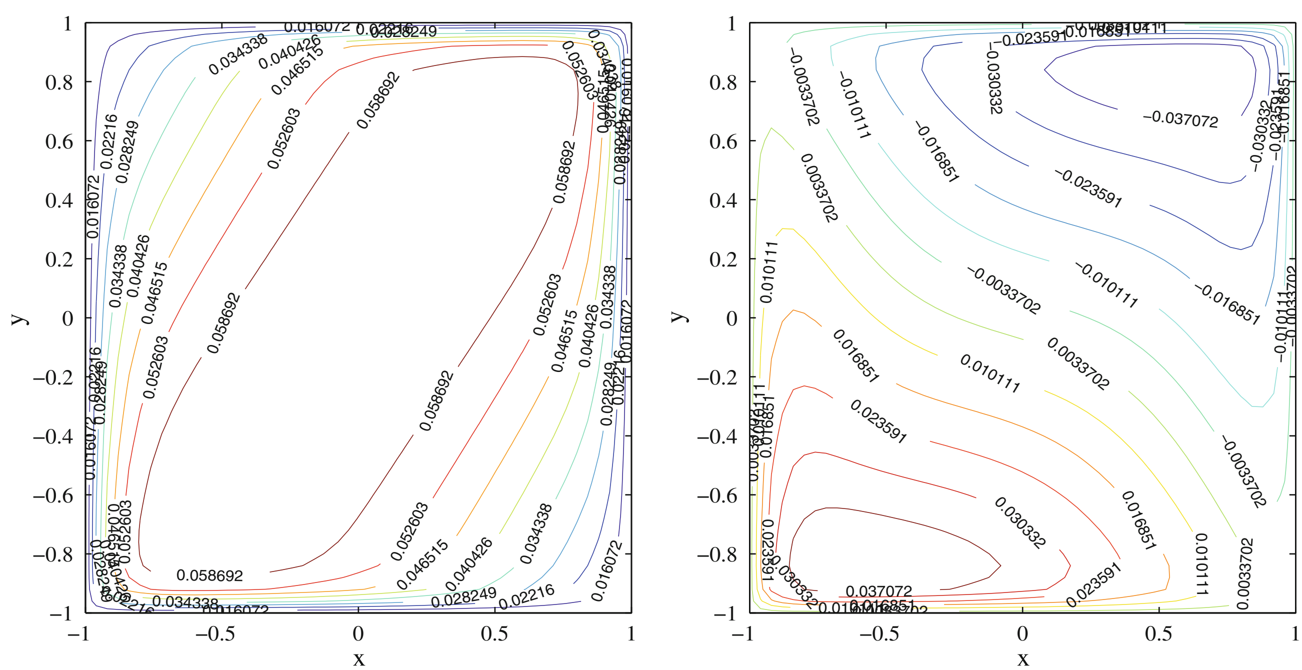

Fig. 10 The contour plot of velocity (*left*) and induced magnetic field (*right*) for $M = 20$, $\lambda = \infty$ and $\theta = \frac{\pi}{3}$

Fig. 6, the contour plots of velocity and the induced magnetic field with $M = 20$ are depicted. From this figure, it can be observed that for high conducting wall case, the induced magnetic field contours are perpendicular to the walls.

Also, Figs. 7 and 8 are plotted to investigate the effect of wall conductivity, λ for both the velocity and induced magnetic field. The graphs along the x-axes tend to the case $\lambda = \infty$ as λ increases.

5.3 Test 3: ducts under oblique magnetic field, $\theta > 0$

In this case, we consider the MHD equation that by using externally applied magnetic field, makes angle θ with the

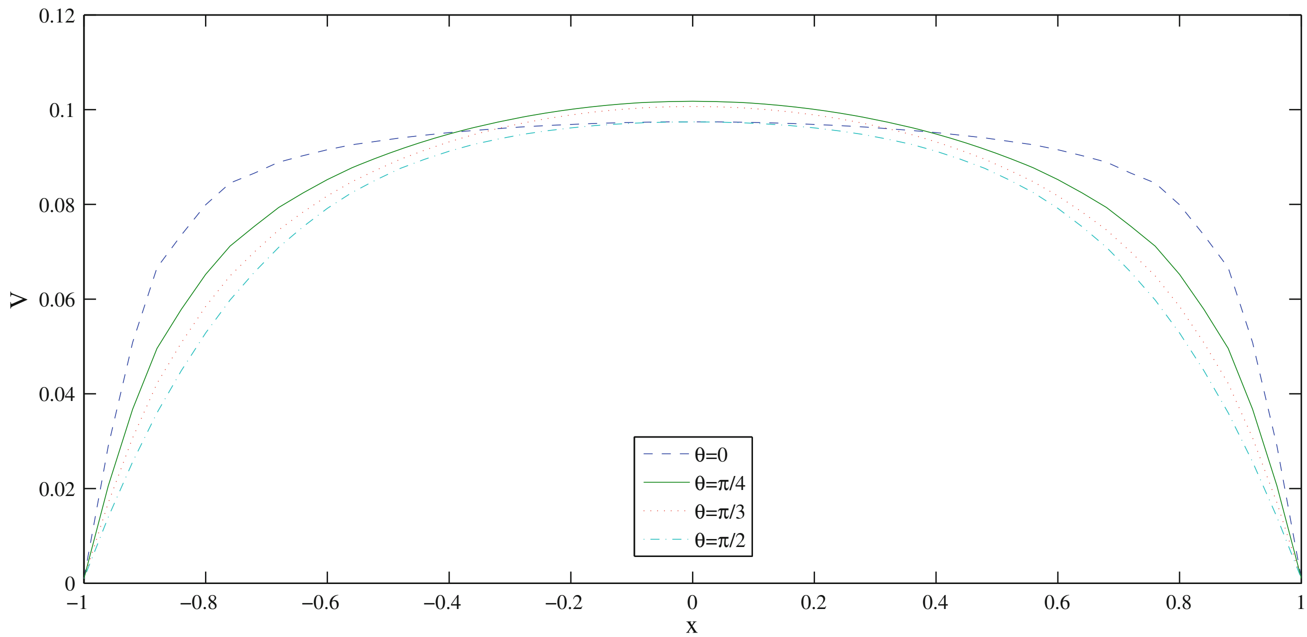

Fig. 11 Plot of velocity along the x-axes ($y = 0$) for $M = 10,\ \lambda = \infty$ and different values of θ

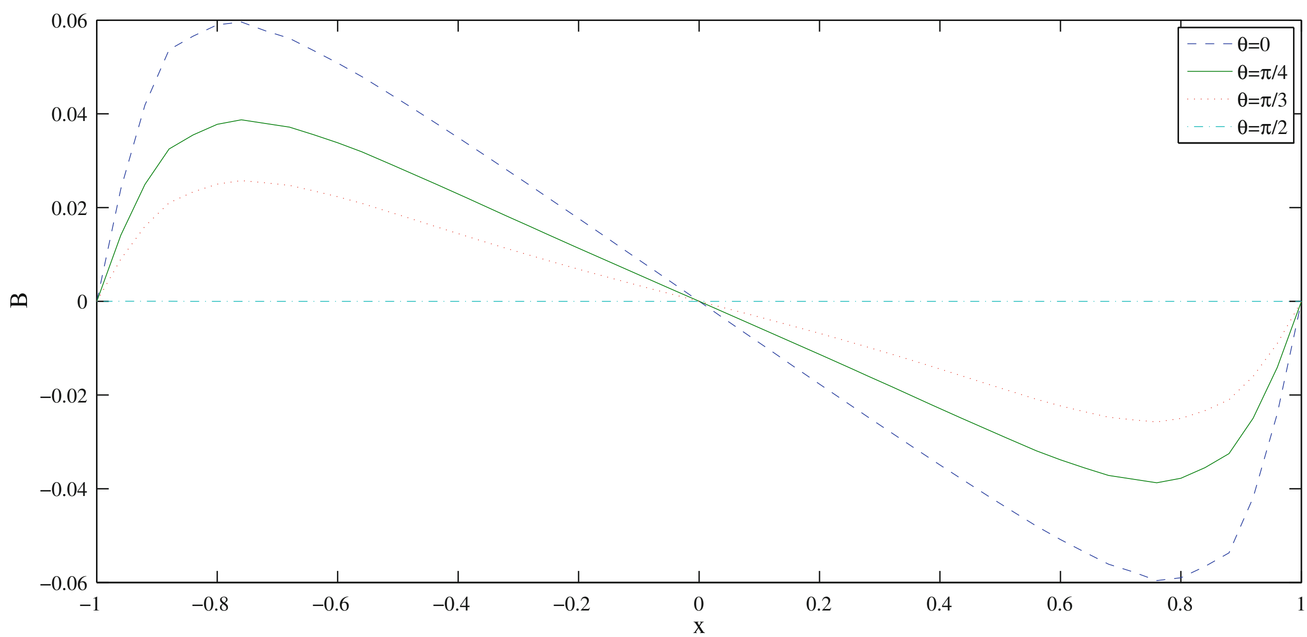

Fig. 12 Plot of induced magnetic field along the x-axes ($y = 0$) for $M = 10,\ \lambda = \infty$ and different values of θ

x-axes. The contour plots for $M = 20, \lambda = \infty, \theta = \frac{\pi}{4}$, and $\theta = \frac{\pi}{3}$ are graphed in Figs. 9 and 10, respectively. Figures 11 and 12 demonstrate the effect of different values of θ along the x-axes for $M = 10,\ \lambda = \infty$. The graphs show that the induced magnetic field along the x-axes decreases when θ increases from 0 to $\frac{\pi}{2}$.

5.4 Test 4: ducts with $M = 0, \lambda, \theta =$ arbitrary

Finally, we consider MHD equation with $M = 0$. The exact solution of this case has been obtained by Singh and Lal [52]. Clearly, in this test problem, the velocity and induced magnetic field results are independent of λ and θ. The values of

Table 4 Comparison of velocity field of Shercliff's problem at $M = 0$ using FVE method [48], FVSE method [48] and MWS method

(x, y)	Exact value	FVE method $N = 722$	FVSE method $N = 162$	MWS $N = 441$
(0.00, 0.00)	0.294685413	0.292268617	0.294639646	0.294211214
(0.25, 0.00)	0.278882332	0.277749251	0.278837322	0.278435000
(0.50, 0.00)	0.229339626	0.227641472	0.229310695	0.229839018
(0.75, 0.00)	0.139729128	0.138616943	0.139718764	0.139445092
(0.00, 0.25)	0.278882332	0.277749251	0.278826724	0.278261119
(0.25, 0.25)	0.264148031	0.264140337	0.264093068	0.264560730
(0.50, 0.25)	0.217799304	0.217023600	0.217760813	0.218317699
(0.75, 0.25)	0.133327705	0.132722756	0.133311067	0.133946130
(0.00, 0.50)	0.229339629	0.227641472	0.229284974	0.229839015
(0.25, 0.50)	0.217799304	0.217023600	0.217744528	0.217831769
(0.50, 0.50)	0.181144632	0.179895157	0.181102961	0.181719238
(0.75, 0.50)	0.112736689	0.111849409	0.112715493	0.113457367
(0.00, 0.75)	0.139729128	0.138616943	0.139689585	0.139445086
(0.25, 0.75)	0.133327705	0.132722756	0.133288009	0.133946124
(0.50, 0.75)	0.112736685	0.111849409	0.112704285	0.113457359
(0.75, 0.75)	0.072819791	0.072124775	0.072803408	0.072568704

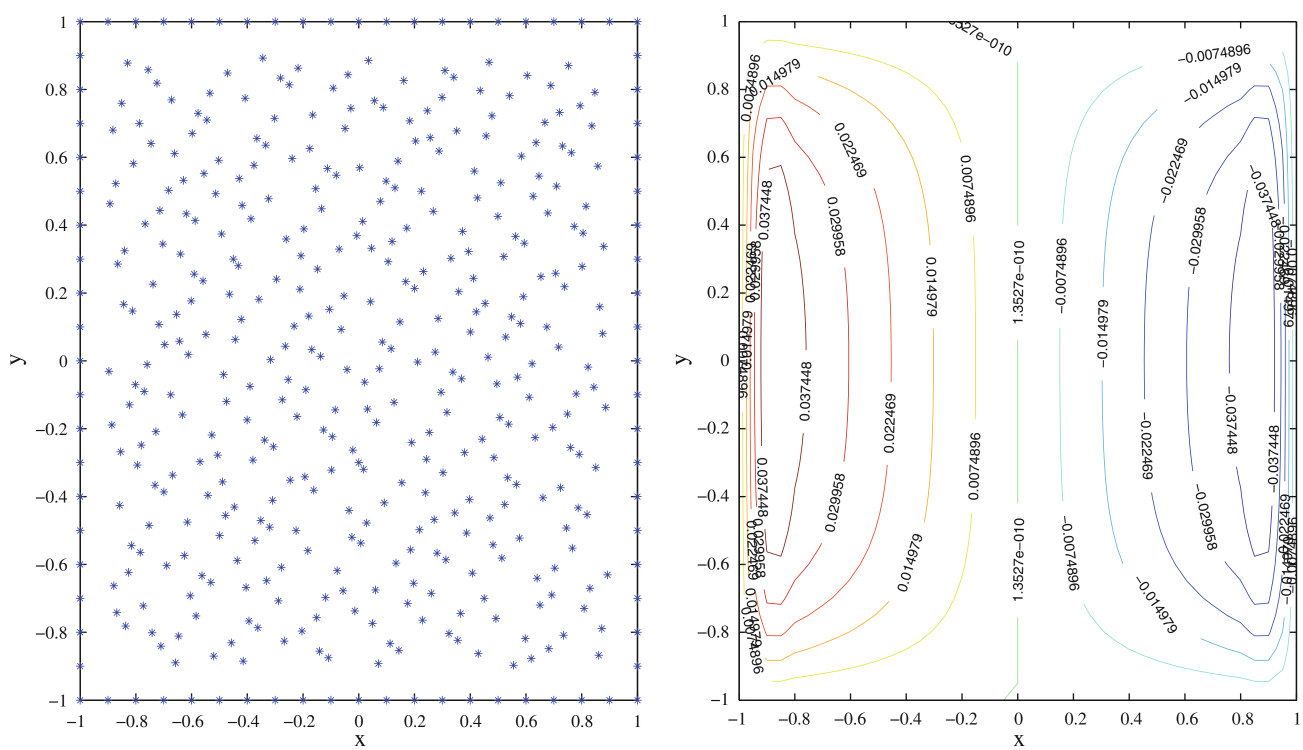

Fig. 13 Irregular nodal distribution and contour plots of the induced magnetic field for $M = 20$

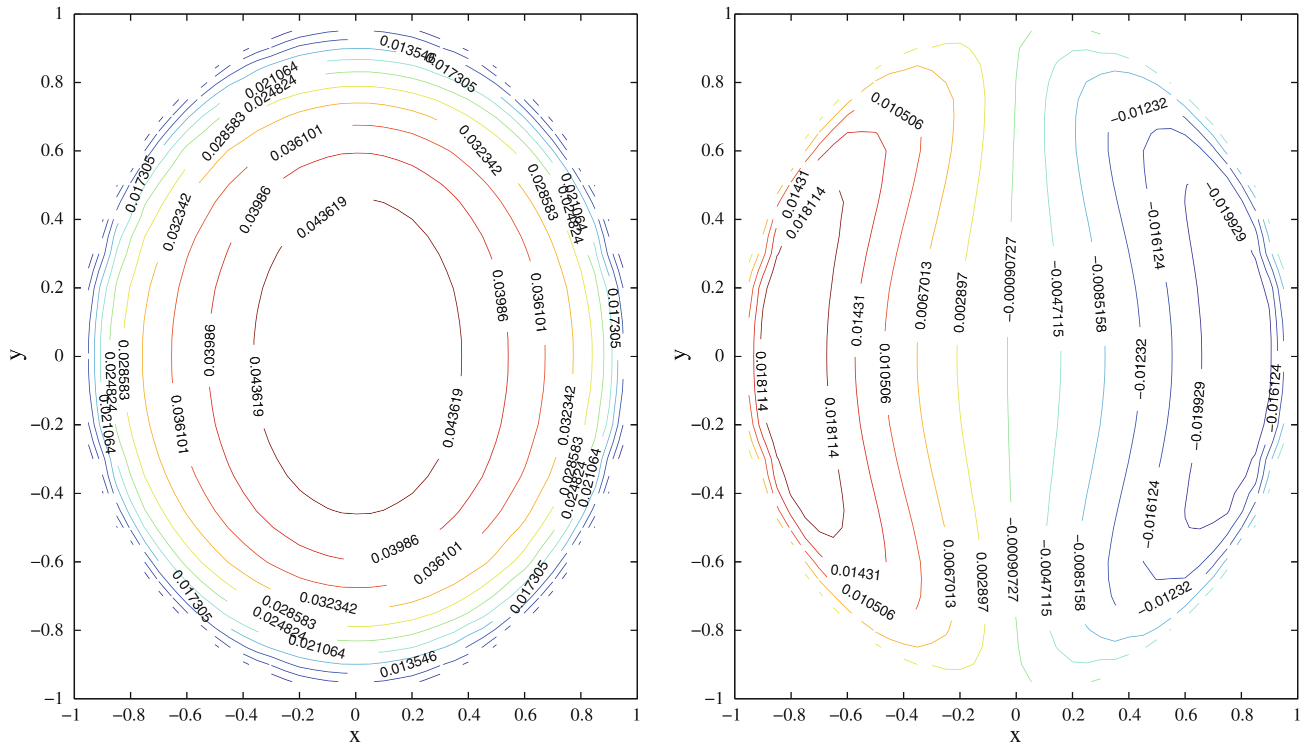

Fig. 14 Contour plots of velocity (*left*) and induced magnetic field (*right*) for $M = 20$ at $t = 0.05$

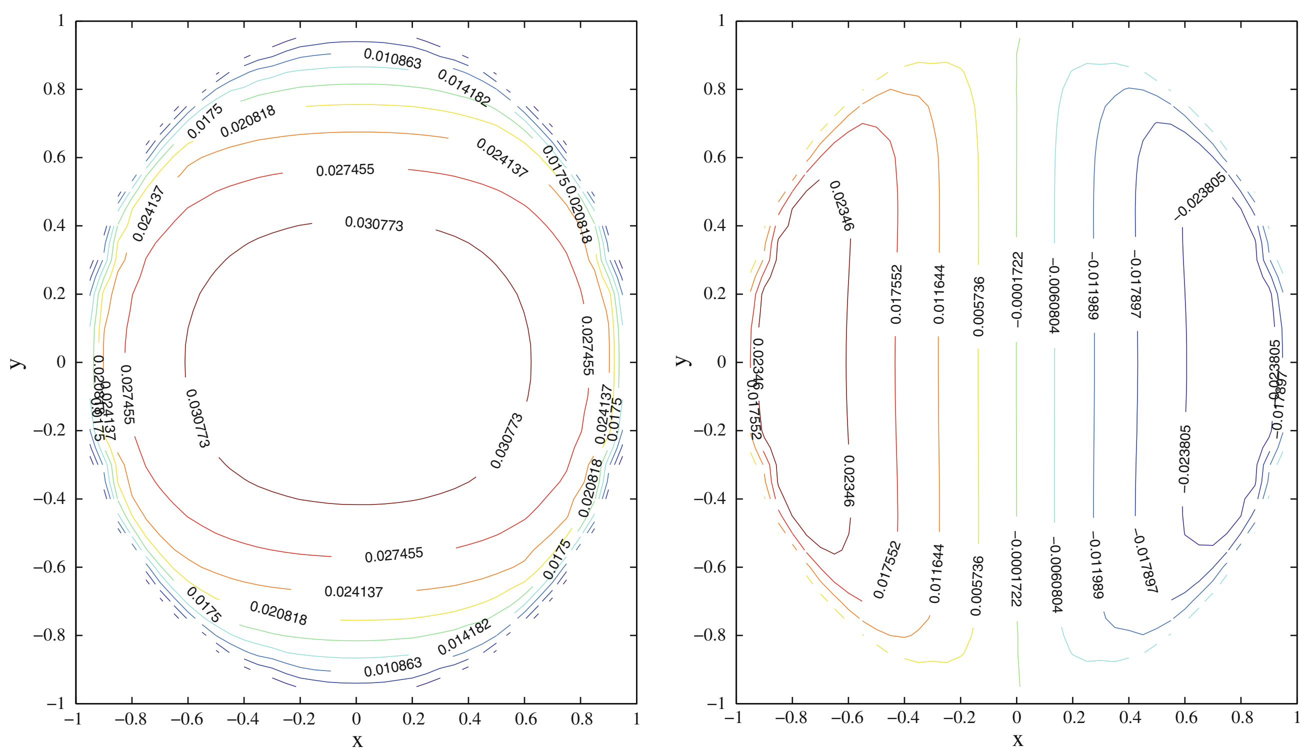

Fig. 15 Contour plots of velocity (*left*) and induced magnetic field (*right*) for $M = 40$ at $t = 0.05$

Table 5 Numerical solution of velocity for selected points at different times for circular pipes at $M = 5$

	(x, y)	$t = 0.1$	$t = 0.2$	$t = 0.5$	$t = 1.0$	Steady state
V	(0.0, 0.0)	0.0916	0.1337	0.1525	0.1530	0.1530
	(1/3, 0.0)	0.0863	0.1261	0.1460	0.1466	0.1466
	(2/3, 0.0)	0.0654	0.0967	0.1161	0.1165	0.1165
	(0.0, 2/3)	0.0632	0.0835	0.0913	0.0918	0.0918
–B	(0.0, 0.0)	0.0000	0.0000	0.0000	0.0000	0.0000
	(1/3, 0.0)	0.0103	0.0272	0.0403	0.0408	0.0408
	(2/3, 0.0)	0.0199	0.0445	0.0621	0.0624	0.0624

velocity at different time levels are compared with the exact solution in Table 4. The obtained results show the accuracy of the proposed method (Fig. 13).

5.5 Test 5: circular pipes with insulating walls, $\lambda = \infty$ and $\theta = 0$

As an example of an irregular cross section, we studied the case of a circular cross section, $x^2 + y^2 \leq 1$. An arbitrary node distribution is considered which is one of the advantages of using meshfree methods. The numerical solution for flow on a circular pipes for Hartmann numbers $M = 20$ and 40, are presented in Figs. 14 and 15, respectively. It observes from the figures that the velocity and induced magnetic filed behave similar to rectangular ones. In Table 5, the numerical results of the velocity and induced magnetic fields are given at different times for $M = 5$, it can be seen that the numerical results are in a good agreement with the steady state solution as time increasing.

6 Conclusion

In this work, the MWS form method is employed for solving the unsteady two dimensional magnetic hydrodynamic flow in rectangular and circular pipes. The MWS form method applied the moving least square approximation and radial point interpolation to construct the shape functions. But, since the MLSRKP scheme was given as a different version of the moving least square method, the MLSRKP approximation is used to approximate the unknown functions. Moreover, a time stepping method is applied to deal with the time derivatives. The numerical results are presented for MHD duct problems with various values of θ, orientation of applied magnetic field with x-axes, λ, the wall conductivity and M, the Hartmann number. The figures are depicted to simulate the effect of these parameters. The numerical results are compared with three other methods in the cases with steady state solutions. In these cases, comparisons reveal that the new method is accurate and agrees with the exact solutions.

Acknowledgments The authors are very grateful to the reviewers for carefully reading this paper and for their comments and suggestions which have improved the paper.

References

1. Alfvén H (1942) Existence of electromagnetic-hydrodynamic waves. Nature 150:405–406
2. Atluri SN (2004) The meshless method (MLPG) for domain and BIE discretizations. Tech Science Press
3. Atluri SN, Zhu T (1998) A new meshless local Petrov–Galerkin (MLPG) approach in computational mechanics. Comput Mech 22:117–127
4. Atluri SN, Kim HG, Cho JY (1999) A critical assessment of the truly meshless local Petrov–Galerkin (MLPG) and local boundary integral equation (LBIE) methods. Comput Mech 24:348–372
5. Atluri SN, Shen S (2002) The meshless local Petrov–Galerkin (MLPG) method: a simple and less-costly alternative to the finite element and boundary element methods. CMES: Comp Model Eng Sci 3:11–51
6. Belytschko T, Lu YY, Gu L (1994) Element-free Galerkin methods. Int J Numer Meth Eng 37:29–56
7. Belytschko T, Lu YY, Gu L (1994) Element-free Galerkin methods. Intern J Numer Methods Eng 37(2):229–256
8. Bourantas GC, Skouras ED, Loukopoulos VC, Nikiforidis GC (2009) An accurate, stable and efficient domain-type meshless method for the solution of MHD flow problems. J Comput Phys 228:8135–8160
9. Bozkaya C, Tezer-Sezgin M (2007) Fundamental solution for coupled magnetohydrodynamic flow equations. J Comput Appl Math 203:125–144
10. Chang C, Lundgren TS (1961) Duct flow in magnetohydrodynamics. ZAMP 12:100–114
11. Dehghan M (2006) Finite difference procedures for solving a problem arising in modeling and design of certain optoelectronic devices. Math Comput Simul 71:16–30
12. Dehghan M, Shokri A (2008) A numerical method for solution of the two-dimensional sine-Gordon equation using the radial basis functions. Math Comput Simul 79:700–715
13. Dehghan M, Mirzaei D (2009) Meshless local boundary integral equation (LBIE) method for the unsteady magnetohydrodynamic (MHD) flow in rectangular and circular pipes. Comput Phys Commun 180:1458–1466
14. Dehghan M, Mirzaei D (2009) Meshless local Petrov–Galerkin (MLPG) method for the unsteady magnetohydrodynamic (MHD) flow through pipe with arbitrary wall conductivity. Appl Numer Math 59:1043–1058
15. Dehghan M, Shokri A (2009) Numerical solution of the nonlinear Klein–Gordon equation using radial basis functions. J Comput Appl Math 230:400–410

16. Dehghan M, Ghesmati A (2010) Combination of meshless local weak and strong (MLWS) forms to solve the two dimensional hyperbolic telegraph equation. Eng Anal Bound Elem 34:324–336
17. Dehghan M, Ghesmati A (2010) Numerical simulation of two-dimensional sine-Gordon solitons via a local weak meshless technique based on the radial point interpolation method (RPIM). Comput Phys Commun 181:772–786
18. Dehghan M, Sabouri M (2012) A spectral element method for solving the Pennes bioheat transfer equation by using triangular and quadrilateral elements. Appl Math Model 36:6031–6049
19. Dehghan M, Nikpour A (2013) The solitary wave solution of coupled Klein–Gordon–Zakharov equations via two different numerical methods. Comput Phys Commun 184:2145–2158
20. Dragos L (1975) Magneto-fluid dynamics. Abacus Press, England
21. Duarte CA, Oden JT (1996) H-p clouds-an h-p meshless method. Numer Meth Partial Diff Equ 12(6):673–705
22. Franke R, Nielson G (1980) Smooth interpolation of large sets of scattered data. Int J Numer Meth Eng 15:1691–1704
23. Gingold R, Monaghan J (1977) Smoothed particle hydrodynamics: theory and application to non spherical stars. Mon Not R Astr Soc 181:375–389
24. Gold RR (1962) Magnetohydrodynamic pipe flow. Part 1. J Fluid Mech 13:505–512
25. Gosz J, Liu WK (1996) Admissible approximations for essential boundary conditions in the reproducing kernel particle method. Comput Mech 19:120–135
26. Gu YT, Liu GR (2005) A meshfree weak-strong (MWS) form method for time dependent problems. Comput Mech 35:134–145
27. Gupta SC, Singh B (1972) Unsteady MHD flow in a rectangular channel under transverse magnetic field. Indian J Pure Appl Math 3:1038–1047
28. Hartmann J, Hg-Dynamics I (1937) Theory of the laminar flow of an electrically conducting liquid in a homogeneous magnetic field. K Dan Vidensk Selsk Mat Fys Medd 15:1–27
29. Hartmann J, Lazarus F (1937) Experimental investigations on the flow of mercury in a homogeneous magnetic field. K Dan Vidensk Selsk Mat Fys Medd 15:1–45
30. Hosseinzadeh H, Dehghan M, Mirzaei D (2013) The boundary element method for magneto-hydrodynamic (MHD) channel flows at high Hartmann numbers. Appl Math Model 37:2337–2351
31. Huang Z (2009) Tailored finite point method for the interface problem. Netw Hetergenous Media 4:91–106
32. Kwon KC, Park SH, Jiang BN, Youn SK (2003) The least-squares meshfree method for solving linear elastic problems. Comput Mech 30:196–211
33. Li S, Liu WK (1996) Moving least square reproducing kernel method part II: fourier analysis. Comput Meth Appl Mech Eng 139:159–194
34. Li S, Liu WK (2007) Meshfree particle methods. Springer, Berlin
35. Liu WK, Jun S, Zhang YF (1995) Reproducing kernel particle methods. Intern J Numer Meth Fluids 20(8–9):1081–1106
36. Liu WK, Jun S, Zhang YF (1995) Reproducing kernel particle methods for structural dynamics. Intern J Numer Meth Eng 38:1655–1679
37. Liu WK, Li S, Belytschko T (1997) Moving least-square reproducing kernel methods (I) methodology and convergence. Comput Meth Appl Mech Eng 143:113–154
38. Liu WK, Uras RA, Chen Y (1997) Enrichment of the finite element method with the reproducing kernel particle method. J Appl Mech ASME 64:861–870
39. Liu GR, Gu YT (2002) A truly meshless method based on the strong-weak form. In: Liu GR (ed) Advances in meshfree and X-FEM methods. World Scientific, Singapore, pp 259–261
40. Liu GR, Gu YT (2003) A meshfree method: meshfree weak-strong (MWS) form method for 2-D solids. Comput Mech 33:2–14
41. Liu GR, Wu YL, Ding H (2004) Meshfree weak-strong (MWS) form method and its application to incompressible flow problems. Int J Numer Meth Fluids 46:1025–1047
42. Loukopoulos VC, Bourantas GC, Skouras ED, Nikiforidis GC (2011) Localized meshless point collocation method for time-dependent magnetohydrodynamics flow through pipes under a variety of wall conductivity conditions. Comput Mech 2:137–159
43. Melenk JM, Babuska I (1996) The partition of unity finite element method: basic theory and applications. Comput Methods Appl Mech Eng 139(1–4):289–314
44. Nayroles B, Touzot G, Villon P (1992) Generalizing the finite element method: diffuse approximation and diffuse elements. Comput Mech 10(5):307–318
45. Oñate E, Idelsohn S, Zienkiewicz OC, Taylor RL, Sacco C (1996) A finite point method for analysis of fluid mechanics problems. Applications to convective transport and fluid flow. Int J Numer Methods Eng 39:3839–3866
46. Salah NB, Soulaimani WG, Habashi WG (2001) A finite element method for magnetohydrodynamic. Comput Methods Appl Mech Eng 190:5867–5892
47. Salehi R, Dehghan M (2013) A moving least square reproducing polynomial meshless method. Appl Numer Math 69:34–58
48. Shakeri F, Dehghan M (2011) A finite volume spectral element method for solving magnetohydrodynamic (MHD) equations. Appl Numer Math 61:1–23
49. Shercliff JA (1953) Steady motion of conducting fluids in pipes under transverse magnetic fields. Proc Camb Phil Soc 49:136–144
50. Sheu TWH, Lin RK (2004) Development of a convection-diffusion-reaction magnetohydrodynamic solver on nonstaggered grids. Int J Numer Meth Fluids 45:1209–1233
51. Shokri A, Dehghan M (2012) Meshless method using radial basis functions for the numerical solution of two-dimensional complex Ginzburg-Landau equation. Comput Model Eng Sci CMES 34:333–358
52. Singh B, Lal J (1982) Finite element method in MHD channel flow problems. Int J Numer Meth Eng 18:1091–1111
53. Singh B, Lal J (1984) Finite element method of MHD channel flow with arbitrary wall conductivity. J Math Phys Sci 18:501–516
54. Tatari M, Dehghan M (2009) On the solution of the non-local parabolic partial differential equations via radial basis functions. Appl Math Model 33:1729–1738
55. Tatari M, Kamranian M, Dehghan M (2011) The finite point method for reaction-diffusion systems in developmental biology. Comput Model Eng Sci CMES 82:1–27
56. Tezer-Sezgin M, Köksal S (1989) Finite elemen tmethod for solving MHD flow in a rectangular duct. Int J Numer Meth Eng 28:445–459
57. Tezer-Sezgin M (1994) Boundary element methods solution of MHD flow in a rectangular duct. Int J Numer Meth Fluids 18:937–952
58. Tezer-Sezgin M, Han Aydin S (2006) Solution of magnetohydrodynamic flow problems using the boundary element method. Eng Anal Bound Elem 30:411–418
59. Tezer-Sezgin M, Bozkaya C (2008) Boundary element method solution of magnetohydrodynamic flow in a rectangular duct with conducting walls parallel to applied magnetic field. Comput Mech 41:769–775
60. Verardi SLL, Machado JM, Cardoso JR (2002) The element-free Galerkin method applied to the study of fully developed magneto-hydrodynamic duct flows. IEEE Trans Magn 38:941–944
61. Verardi SLL, Machado JM, Shiyou Y (2003) The application of interpolating MLS approximations to the analysis of MHD flows. Finite Elem Anal Des 39:1173–1187

62. Wang S, Zhang H (2011) Partition of unity-based thermomechanical meshfree method for two-dimensional crack problems. Arch Appl Mech 81:1351–1363

63. Zahiri S, Daneshmand F, Akbari MH (2009) Using meshfree weak-strong form method for a 2-D heat transfer problem. ASME Conference Proceedings, pp 643–651